Computer-Aided Civil and Infrastructure Engineering **23** (2008) 373–388

Modal Identification Study of Vincent Thomas Bridge Using Simulated Wind-Induced Ambient Vibration Data

Xianfei He, Babak Moaveni, Joel P. Conte* & Ahmed Elgamal

Department of Structural Engineering, University of California at San Diego, USA

&

Sami F. Masri

Department of Civil and Environmental Engineering, University of Southern California, USA

Abstract: *In this article, wind-induced vibration response of Vincent Thomas Bridge, a suspension bridge located in San Pedro near Los Angeles, California, is simulated using a detailed three-dimensional finite element model of the bridge and a state-of-the-art stochastic wind excitation model. Based on the simulated wind-induced vibration data, the modal parameters (natural frequencies, damping ratios, and mode shapes) of the bridge are identified using the data-driven stochastic subspace identification method. The identified modal parameters are verified by the computed eigenproperties of the bridge model. Finally, effects of measurement noise on the system identification results are studied by adding zero-mean Gaussian white noise processes to the simulated response data. Statistical properties of the identified modal parameters are investigated under an increasing level of measurement noise. The framework presented in this article will allow us to investigate the effects of various realistic damage scenarios in long-span cable-supported (suspension and cable-stayed) bridges on changes in modal identification results. Such studies are required to develop robust and reliable vibration-based structural health monitoring methods for this type of bridge, which is a long-term research objective of the authors.*

*To whom correspondence should be addressed. E-mail: *jpconte@ucsd.edu*.

1 INTRODUCTION

Vibration-based structural health monitoring has been the subject of significant research in structural engineering in recent years. The basic premise of vibration-based structural health monitoring is that changes in structural characteristics such as mass, stiffness, and energy dissipation mechanisms influence the vibration response characteristics of structures. Therefore, changes in dynamic features such as modal parameters and quantities derived thereof are often used as damage indicators in structural damage identification and health monitoring. Salawu (1997) presented a review on the use of natural frequency changes for damage detection. It is, however, challenging if not impossible to localize the detected damage (e.g., to obtain spatial information on the damage) from changes in natural frequencies only. Pandey et al. (1991) introduced the concept of mode shape curvature for damage localization. In their study, both a cantilever and a simply supported beam model were used to demonstrate the effectiveness of using changes in modal curvature as a damage indicator to detect and localize damage. As another mode shape based damage indicator, Pandey and Biswas (1994) proposed the use of changes in the dynamically measured flexibility matrix to detect and localize damage. They showed that

the flexibility matrix of a structure can be easily and accurately estimated from a few low-frequency vibration modes of the structure. Methods based on changes in identified modal parameters to detect and localize damage in structures have also been further developed for the purpose of damage quantification (i.e., estimation of the extent of damage). Among these methods are strain-energy based methods (Shi et al., 2002), the direct stiffness calculation method (Maeck and De Roeck, 1999), and sensitivity-based finite element (FE) model updating methods (Friswell and Mottershead, 1995; Teughels and De Roeck, 2004). A comprehensive literature survey on vibration-based structural health monitoring methods can be found in a number of recent publications (Doebling et al., 1996; Farrar and Jauregui, 1998; Sohn et al., 2003).

To develop a robust and reliable structural health monitoring methodology, it is essential to investigate the effects of realistic damage scenarios on structural modal properties. Because it is inconvenient or impossible to study the changes in structural modal parameters caused by various damage scenarios and damage levels through actual tests on a real structure during its service life, dynamic response simulation of the structure based on a well calibrated and validated FE model thereof provides an essential tool in structural health monitoring research. In this article, a simulation platform is presented to simulate the wind-induced (ambient) vibration response of Vincent Thomas Bridge (VTB) using a detailed three-dimensional (3D) FE model of the bridge and a state-of-the-art stochastic wind excitation model. The VTB is a suspension bridge that crosses over the main channel of Los Angeles Harbor in San Pedro, California. The bridge was constructed in the early 1960s with an overall length of approximately 1850 m, comprising the main span of 457 m and 154 m spans on either side. Generally, traffic, wind, microtremors, and their combinations are the main sources of ambient excitation for bridges. This article focuses on realistic simulation of the wind-induced response of VTB and system identification of the bridge based on its simulated wind response data.

Wind loads, including self-excited (caused by the interaction between wind and structural motion) and buffeting forces (caused by the fluctuating wind velocity field), are dependent on the geometric configuration of the bridge deck section, the reduced frequency of the bridge, and the incoming wind velocity fluctuations. In the simulation, the self-excited forces are represented in the time domain by means of convolution integrals involving aerodynamic impulse functions and structural motions. To simulate properly the stochastic characteristics of buffeting forces, the longitudinal (along-wind direction) and vertical spatially discrete wind velocity fields along the bridge axis are simulated as two independent stochastic vector processes according to their prescribed power spectral density matrices. The spectra of the longitudinal and vertical wind velocity fields are assumed to remain constant along the bridge axis and the coherence function of the wind velocity fluctuations at two different positions along the bridge is taken as the model proposed by Davenport (1968).

In the second part of the article, the dynamic properties of the bridge are identified using the data-driven stochastic subspace identification method (Van Overschee and De Moor, 1996) based on the low-amplitude simulated wind-induced response of VTB. The system identification results are verified by the computed eigenproperties of the bridge FE model, which allows us to assess the performance of the above output-only system identification method when applied to wind-excited long-span suspension bridges. To study the effects of measurement noise on the system identification results, zero-mean Gaussian white noise processes are added to the simulated output signals. Statistical properties (bias and coefficient of variation) of the identified modal parameters are investigated under increasing levels of measurement noise.

The framework presented in this article will allow us to investigate systematically the effects of various realistic damage scenarios in long-span cable-supported bridges on changes in modal identification results obtained from ambient vibration data. Such studies are required to develop robust and reliable vibration-based structural health monitoring methods for this type of bridge, which is a long-term research objective of the authors.

2 AERODYNAMIC FORCES

2.1 Self-excited forces

The differential equations of motion of a bridge subjected to aerodynamic forces with respect to the static equilibrium position can be expressed as

$$\mathbf{M}\,\ddot{\mathbf{x}}(t) + \mathbf{C}\,\dot{\mathbf{x}}(t) + \mathbf{K}\,\mathbf{x}(t) = \mathbf{F}(t) = \mathbf{F}_{se}(t) + \mathbf{F}_{b}(t) \quad (1)$$

where $\mathbf{x}(t), \dot{\mathbf{x}}(t)$, and $\ddot{\mathbf{x}}(t)$ = nodal displacement, velocity, and acceleration response vectors, respectively; $\mathbf{M}$, $\mathbf{C}$, and $\mathbf{K}$ = structural mass, damping, and stiffness matrices, respectively; $\mathbf{F}$ = nodal load vector, and the subscripts *se* and *b* denote the self-excited and buffeting aerodynamic force components, respectively.

For harmonic structural motion, the self-excited forces such as lift L_{se}, drag D_{se}, and pitching moment M_{se} (see Figure 1) per unit span of the bridge are typically expressed as (Scanlan, 1978a; Simiu and Scanlan, 1996; Chen et al., 2000a, 2000b)

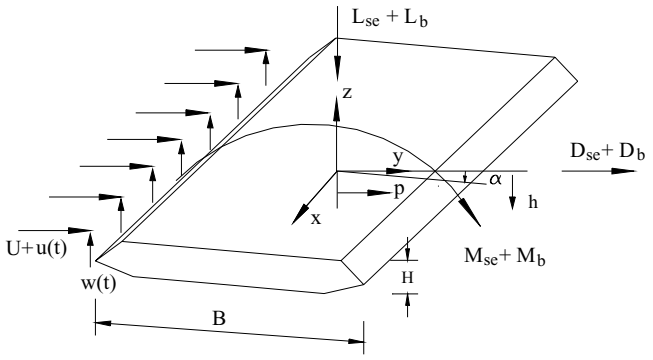

Fig. 1. Aerodynamic forces on bridge deck section.

$$L_{se}(t) = \frac{1}{2}\rho U^2 B\left[KH_1^*\frac{\dot{h}}{U} + KH_2^*\frac{B\dot{\alpha}}{U} + K^2H_3^*\alpha + K^2H_4^*\frac{h}{B} + KH_5^*\frac{\dot{p}}{U} + K^2H_6^*\frac{p}{B}\right] \tag{2a}$$

$$D_{se}(t) = \frac{1}{2}\rho U^2 B\left[KP_1^*\frac{\dot{p}}{U} + KP_2^*\frac{B\dot{\alpha}}{U} + K^2P_3^*\alpha + K^2P_4^*\frac{p}{B} + KP_5^*\frac{\dot{h}}{U} + K^2P_6^*\frac{h}{B}\right] \tag{2b}$$

$$M_{se}(t) = \frac{1}{2}\rho U^2 B^2\left[KA_1^*\frac{\dot{h}}{U} + KA_2^*\frac{B\dot{\alpha}}{U} + K^2A_3^*\alpha + K^2A_4^*\frac{h}{B} + KA_5^*\frac{\dot{p}}{U} + K^2A_6^*\frac{p}{B}\right] \tag{2c}$$

where ρ = air density; U = mean wind velocity; B = bridge deck width; ω = circular frequency of vibration; $K = \omega B/U$ = reduced frequency; H_i^*, A_i^* and P_i^* ($i = 1,\ldots,6$) = flutter derivatives; and h, p, and α = vertical, lateral, and torsional displacement, respectively. It should be noted that the formulation of the self-excited forces in Equation (2) cannot be applied directly in time domain simulation, as the flutter derivatives are frequency dependent. For arbitrary structural motion, the self-excited forces per unit span can be expressed in terms of impulse response functions as (Lin and Yang, 1983; Chen et al., 2000a, 2000b)

$$L_{se}(t) = \frac{1}{2}\rho U^2\left[\int_{-\infty}^{t} f_{Lh}(t-\tau)h(\tau)\,d\tau + \int_{-\infty}^{t} f_{Lp}(t-\tau)p(\tau)\,d\tau + \int_{-\infty}^{t} f_{L\alpha}(t-\tau)\alpha(\tau)\,d\tau\right] \tag{3a}$$

$$D_{se}(t) = \frac{1}{2}\rho U^2\left[\int_{-\infty}^{t} f_{Dh}(t-\tau)h(\tau)\,d\tau + \int_{-\infty}^{t} f_{Dp}(t-\tau)p(\tau)\,d\tau + \int_{-\infty}^{t} f_{D\alpha}(t-\tau)\alpha(\tau)\,d\tau\right] \tag{3b}$$

$$M_{se}(t) = \frac{1}{2}\rho U^2\left[\int_{-\infty}^{t} f_{Mh}(t-\tau)h(\tau)\,d\tau + \int_{-\infty}^{t} f_{Mp}(t-\tau)p(\tau)\,d\tau + \int_{-\infty}^{t} f_{M\alpha}(t-\tau)\alpha(\tau)\,d\tau\right] \tag{3c}$$

where the $f_{Xy}(\cdots)$ terms in the integrands are the impulse response functions of the self-excited forces, which are associated with the aerodynamic force component indicated by the subscript. To evaluate the self-excited forces in the time domain based on Equation (3), it is necessary to determine the aerodynamic impulse response functions based on the experimentally determined flutter derivatives. For this purpose, the self-excited forces are taken to the frequency domain via Fourier transformation of Equations (2) and (3) as

$$\begin{bmatrix} F\ [L_{se}(t)] \\ F\ [D_{se}(t)] \\ F\ [M_{se}(t)] \end{bmatrix} = \frac{1}{2}\rho U^2 \begin{bmatrix} K^2(iH_1^* + H_4^*) & K^2(iH_5^* + H_6^*) & K^2B(iH_2^* + H_3^*) \\ K^2(iP_5^* + P_6^*) & K^2(iP_1^* + P_4^*) & K^2B(iP_2^* + P_3^*) \\ K^2B(iA_1^* + A_4^*) & K^2B(iA_5^* + A_6^*) & K^2B^2(iA_2^* + A_3^*) \end{bmatrix} \cdot \begin{bmatrix} F\ [h(t)] \\ F\ [p(t)] \\ F\ [\alpha(t)] \end{bmatrix} \tag{4}$$

$$\begin{bmatrix} F\ [L_{se}(t)] \\ F\ [D_{se}(t)] \\ F\ [M_{se}(t)] \end{bmatrix} = \frac{1}{2}\rho U^2 \begin{bmatrix} F\ [f_{Lh}(t)] & F\ [f_{Lp}(t)] & F\ [f_{L\alpha}(t)] \\ F\ [f_{Dh}(t)] & F\ [f_{Dp}(t)] & F\ [f_{D\alpha}(t)] \\ F\ [f_{Mh}(t)] & F\ [f_{Mp}(t)] & F\ [f_{M\alpha}(t)] \end{bmatrix} \cdot \begin{bmatrix} F\ [h(t)] \\ F\ [p(t)] \\ F\ [\alpha(t)] \end{bmatrix} \tag{5}$$

where $F[\dots]$ = Fourier transform operator. Thus, the relationship between aerodynamic impulse response functions and flutter derivatives can be obtained by comparing Equations (4) and (5) term by term:

$$\mathcal{F}\ [f_{Lh}(t)] = K^2\left(iH_1^* + H_4^*\right) \tag{6a}$$

$$\mathcal{F}\ [f_{Lp}(t)] = K^2\left(iH_5^* + H_6^*\right) \tag{6b}$$

$$\mathcal{F}\ [f_{L\alpha}(t)] = K^2 B\left(iH_2^* + H_3^*\right) \tag{6c}$$

$$\mathcal{F}\ [f_{Dh}(t)] = K^2\left(iP_5^* + P_6^*\right) \tag{7a}$$

$$\mathcal{F}\ [f_{Dp}(t)] = K^2\left(iP_1^* + P_4^*\right) \tag{7b}$$

$$\mathcal{F}\ [f_{D\alpha}(t)] = K^2 B\left(iP_2^* + P_3^*\right) \tag{7c}$$

$$\mathcal{F}\ [f_{Mh}(t)] = K^2 B\left(iA_1^* + A_4^*\right) \tag{8a}$$

$$\mathcal{F}\ [f_{Mp}(t)] = K^2 B\left(i\,A_5^* + A_6^*\right) \tag{8b}$$

$$\mathcal{F}\ [f_{M\alpha}(t)] = K^2 B^2\left(i\,A_2^* + A_3^*\right) \tag{8c}$$

Using the above equations, the self-excited forces can be used in time domain analysis based on Equation (3) once the flutter derivatives are obtained from wind-tunnel experiments. The experimental flutter derivatives in the above equations are usually obtained at a discrete set of reduced frequencies $K(\omega_k)$. Then, the rational function approximation method known as Roger's approximation is used to estimate the aerodynamic force coefficients defined in Equations (6)–(8), also known as aerodynamic transfer functions, as continuous functions of the reduced frequency K (Roger, 1977; Chen et al., 2000a; Lazzari et al., 2004). For example, let

$$\begin{aligned}\mathcal{F}\ [f_{Lh}(t)] &= K^2\left(iH_1^* + H_4^*\right)\\ &= \left[C_{Lh,1} + iC_{Lh,2}\frac{B\omega}{U} + C_{Lh,3}\left(\frac{iB\omega}{U}\right)^2 + \sum_{k=4}^{n} C_{Lh,k}\frac{i\omega}{\frac{U}{d_{Lh,k}B} + i\omega}\right]\end{aligned} \tag{9}$$

where $C_{Lh,i}$ and $d_{Lh,k}$ ($d_{Lh,k} \geq 0$; $i = 1,\dots,n$ and $k = 4,\dots,n$) = frequency-independent coefficients. The first and second terms on the right-hand side of Equation (9) represent the noncirculatory static-aerodynamics and the aerodynamic damping, respectively; the third term denotes the additional aerodynamic mass, which is usually negligible; and the rational terms represent the unsteady components which lag the velocity term and allow an approximation of the time delays through the positive values of parameters $d_{Lh,k}$. The value of n indicates the level of accuracy in this approximation. Based on Equation (9), the following relations can be derived:

$$H_1^*(v) = \frac{v}{2\pi}\,C_{Lh,2} + \sum_{k=4}^{n}\frac{v^3}{2\pi d_{Lh,k}^2 v^2 + 8\pi^3}\,C_{Lh,k}\,d_{Lh,k} \tag{10a}$$

$$H_4^*(v) = \frac{v^2}{4\pi^2}\,C_{Lh,1} - C_{Lh,3} + \sum_{k=4}^{n}\frac{v^2}{d_{Lh,k}^2 v^2 + 4\pi^2}\,C_{Lh,k} \tag{10b}$$

where $v = 2\pi/K$ = reduced velocity. Therefore, the frequency-independent coefficients $C_{Lh,i}$ and $d_{Lh,k}$ can be determined through least squares fitting of flutter derivatives obtained experimentally at discrete reduced frequencies/velocities. The above rational function representation of the aerodynamic transfer function for the self-excited lift force component induced by the vertical structural motion (see Equation (9)) can be extended into the Laplace domain by introducing the Laplace parameter $s = i\omega$. Then, the self-excited lift force component induced by vertical structural motion can be derived by substituting the inverse Laplace transformation of $\mathcal{F}\ [f_{Lh}(t)]_{(i\omega=s)}$ into the corresponding component in Equation (3) as

$$\begin{aligned}&L_{se,h}(t)\\ &= \frac{1}{2}\rho U^2\left[C_{Lh,1}h(t) + C_{Lh,2}\frac{B}{U}\dot{h}(t) + C_{Lh,3}\frac{B^2}{U^2}\ddot{h}(t) + \sum_{k=4}^{n} C_{Lh,k}\int_{-\infty}^{t} e^{-\frac{d_{Lh,k}U}{B}(t-\tau)}\dot{h}(\tau)\,d\tau\right]\end{aligned} \tag{11}$$

The self-excited lift force components induced by lateral and torsional structural motions can be obtained similarly. Thus, the total self-excited lift force can be expressed as

$$\begin{aligned}L_{se}(t) &= L_{se,h}(t) + L_{se,p}(t) + L_{se,\alpha}(t)\\ &= \frac{1}{2}\rho U^2\left[C_{Lh,1}h(t) + C_{Lh,2}\frac{B}{U}\dot{h}(t) + C_{Lh,3}\frac{B^2}{U^2}\ddot{h}(t) + \sum_{k=4}^{n} C_{Lh,k}\int_{-\infty}^{t} e^{-\frac{d_{Lh,k}U}{B}(t-\tau)}\dot{h}(\tau)\,d\tau\right]\\ &\quad + \frac{1}{2}\rho U^2\left[C_{Lp,1}p(t) + C_{Lp,2}\frac{B}{U}\dot{p}(t) + C_{Lp,3}\frac{B^2}{U^2}\ddot{p}(t) + \sum_{k=4}^{n} C_{Lp,k}\int_{-\infty}^{t} e^{-\frac{d_{Lp,k}U}{B}(t-\tau)}\dot{p}(\tau)\,d\tau\right]\end{aligned}$$

$$+\frac{1}{2}\rho U^2 B\left[C_{L\alpha,1}\alpha(t)+C_{L\alpha,2}\frac{B}{U}\dot{\alpha}(t)+C_{L\alpha,3}\frac{B^2}{U^2}\ddot{\alpha}(t)+\sum_{k=4}^{n}C_{L\alpha,k}\int_{-\infty}^{t}e^{-\frac{d_{L\alpha,k}U}{B}(t-\tau)}\dot{\alpha}(\tau)\,d\tau\right] \quad (12)$$

Formulations for the self-excited drag force $D_{se}(t)$ and self-excited moment $M_{se}(t)$ can be derived similarly. These derivations are not shown here for the sake of brevity.

2.2 Buffeting forces

The buffeting forces per unit span of the bridge are commonly expressed as (Scanlan, 1978b; Simiu and Scanlan, 1996; Chen et al., 2000a, 2000b)

$$L_b(t)=-\frac{1}{2}\rho U^2 B\left\{C_L\,\chi_{Lbu}\frac{2u(t)}{U}+[C'_L+C_D]\,\chi_{Lbw}\frac{w(t)}{U}\right\} \quad (13a)$$

$$D_b(t)=\frac{1}{2}\rho U^2 B\left\{C_D\,\chi_{Dbu}\frac{2u(t)}{U}+C'_{D\,\chi_{Dbw}}\frac{w(t)}{U}\right\} \quad (13b)$$

$$M_b(t)=\frac{1}{2}\rho U^2 B^2\left\{C_M\,\chi_{Mbu}\frac{2u(t)}{U}+C'_{M\,\chi_{Mbw}}\frac{w(t)}{U}\right\} \quad (13c)$$

where C_L, C_D, C_M = mean lift, drag, and moment coefficients, respectively; $C'_L = dC_L/d\alpha$, $C'_D = dC_D/d\alpha$ and $C'_M = dC_M/d\alpha$ (α = angle of attack of the wind); $u(t)$ and $w(t)$ = wind velocity fluctuations in the longitudinal and vertical directions, respectively; χ_{Lbu}, χ_{Lbw}, χ_{Dbu}, χ_{Dbw}, χ_{Mbu}, χ_{Mbw} = aerodynamic admittance transfer functions between wind velocity fluctuations and buffeting forces. Their squared magnitudes are known as aerodynamic admittance functions. Similar to the self-excited forces in Equation (2), the buffeting forces in Equation (13) cannot be used directly in time domain analysis, because the aerodynamic admittance transfer functions are frequency dependent. From Equation (13), the buffeting force spectra can be derived as

$$S_{Lb}(\omega)=\frac{1}{4}\rho^2 U^2 B^2\left\{4C^2_{L|\chi_{Lbu}|^2}S_{uu}(\omega)+[C'_L+C_D]^2|\chi_{Lbw}|^2 S_{ww}(\omega)\right\} \quad (14a)$$

$$S_{Db}(\omega)=\frac{1}{4}\rho^2 U^2 B^2\left\{4C^2_{D|\chi_{Dbu}|^2}S_{uu}(\omega)+C'^2_{D|\chi_{Dbw}|^2}S_{ww}(\omega)\right\} \quad (14b)$$

$$S_{Mb}(\omega)=\frac{1}{4}\rho^2 U^2 B^4\left\{4C^2_{M|\chi_{Mbu}|^2}S_{uu}(\omega)+C'^2_{M|\chi_{Mbw}|^2}S_{ww}(\omega)\right\} \quad (14c)$$

where $S_{uu}(\omega)$, $S_{ww}(\omega)$ = power spectral density functions of longitudinal and vertical wind velocity fluctuations, respectively. It should be noted that the statistical correlation between longitudinal and vertical wind velocity fluctuations is neglected in deriving Equation (14). The aerodynamic admittance functions are assumed to be identical and approximated by the Liepmann function (Liepmann, 1952) as

$$|\chi_r(\omega)|^2=1\Big/\left(1+\frac{\pi\omega B}{U}\right) \quad (15)$$

where the subscript r refers to Lbu, Lbw, Dbu, Dbw, Mbu, and Mbw. Equivalent wind power spectral density functions are defined as

$$S^{eq}_{uu}(\omega)=S_{uu}(\omega)/(1+\pi\omega B/U) \quad (16a)$$

$$S^{eq}_{ww}(\omega)=S_{ww}(\omega)/(1+\pi\omega B/U) \quad (16b)$$

Thus, the buffeting forces can be obtained from the equivalent wind velocity fluctuations simulated using the equivalent wind power spectral density functions as

$$L_b(t)=-\frac{1}{2}\rho U^2 B\left\{C_L\frac{2u^{eq}(t)}{U}+[C'_L+C_D]\frac{w^{eq}(t)}{U}\right\} \quad (17a)$$

$$D_b(t)=\frac{1}{2}\rho U^2 B\left\{C_D\frac{2u^{eq}(t)}{U}+C'_D\frac{w^{eq}(t)}{U}\right\} \quad (17b)$$

$$M_b(t)=\frac{1}{2}\rho U^2 B^2\left\{C_M\frac{2u^{eq}(t)}{U}+C'_M\frac{w^{eq}(t)}{U}\right\} \quad (17c)$$

2.3 Rational function approximation of flutter derivatives

This section illustrates the rational function representation of self-excited force coefficients (see Equations (6)–(8)) through least squares fitting of flutter derivatives determined experimentally at discrete reduced frequencies/velocities (see Equation (10)).

Because the aerodynamic coefficients of VTB are not available, the flutter derivatives H^*_1 to H^*_4 and A^*_1 to A^*_4, determined experimentally for the William Preston Lane Bridge (WPLB) (J. D. Raggett, Personal communication, 2004) located in Baltimore, Maryland, are used for VTB, which is similar in size and design. The remaining dimensionless aerodynamic coefficients are taken as (J. D. Raggett, Personal communication, 2004): $H^*_5 = H^*_6 = 0$, $A^*_5 = A^*_6 = 0$ and $P^*_2 = P^*_3 = P^*_4 = P^*_5 = P^*_6 = 0$; $C_L = 0$, $C_M = 0$, $C_D = 0.162$ (C_D is estimated as 2.5 times the projected frontal area per unit length of the bridge deck normalized by the deck's width); $C'_L \cong K(H^{*2}_1 + H^{*2}_4)^{1/2} = 1.415$, $C'_M \cong K(A^{*2}_1 + A^{*2}_4)^{1/2} = 0.238$ and $C'_D = 0$; and $P^*_1 = -2C_D/K$.

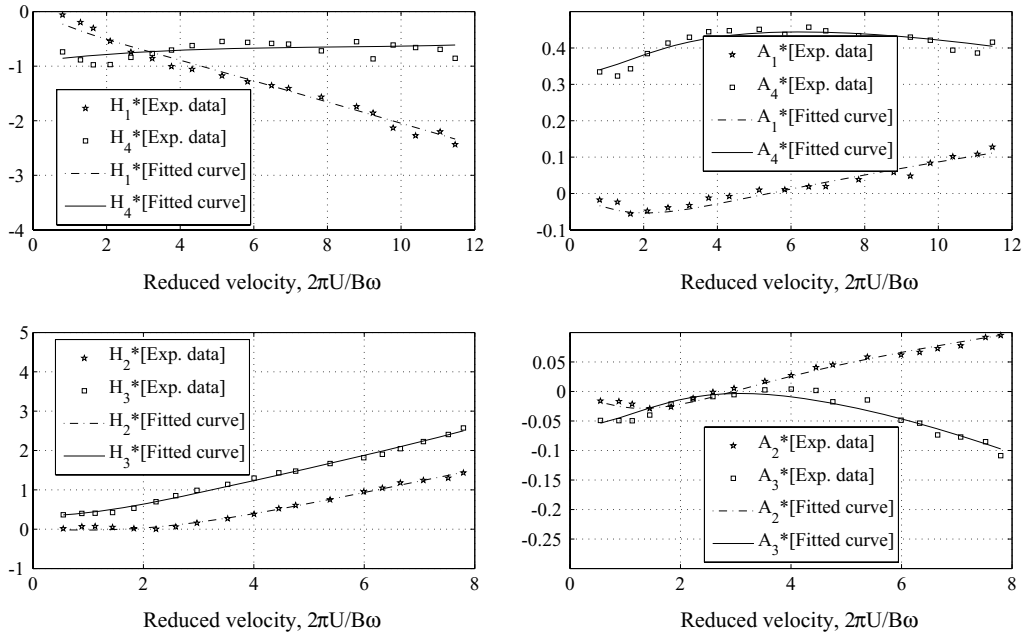

Fig. 2. Rational function approximations of flutter derivatives for William Preston Lane Bridge (J. D. Raggett, Personal communication, 2004).

In this study, two lag terms (i.e., $n = 5$) are used in the rational representations (see Equation (9)). Figure 2 shows a comparison of the flutter derivatives estimated from the rational function representations (e.g., see Equation (10)) and those measured in wind tunnel tests for WPLB. The excellent agreement obtained indicates that the self-excited forces on the bridge deck section can be approximated by the rational functions considered with very good accuracy.

3 SIMULATION OF WIND-INDUCED RESPONSE OF VINCENT THOMAS BRIDGE

A detailed 3D FE model of VTB (see Figure 3) developed in the structural analysis software ADINA (ADINA R&D Inc., 2002) was used in this study for the simulation of the wind-induced response of VTB. This FE model is composed of 3D linear elastic (tension-only) truss elements to represent the main suspension cables and suspender cables, 3D linear elastic membrane and shell elements to model the reinforced-concrete bridge deck, stringers supporting the deck on the floor trusses, and beam-column elements to model the stiffening trusses, the lateral braces between the stiffening trusses and the tower shafts. The floor trusses were modeled with 3D elastic beam-column and truss elements. This FE model consists of approximately 8,900 nodes and 9,400 elements, resulting in approximately 22,000 degrees of freedom (DOFs). The natural frequencies of the low frequency vibration modes computed from this FE model of VTB are given in Table 1 where they are compared with (1) the corresponding natural frequencies

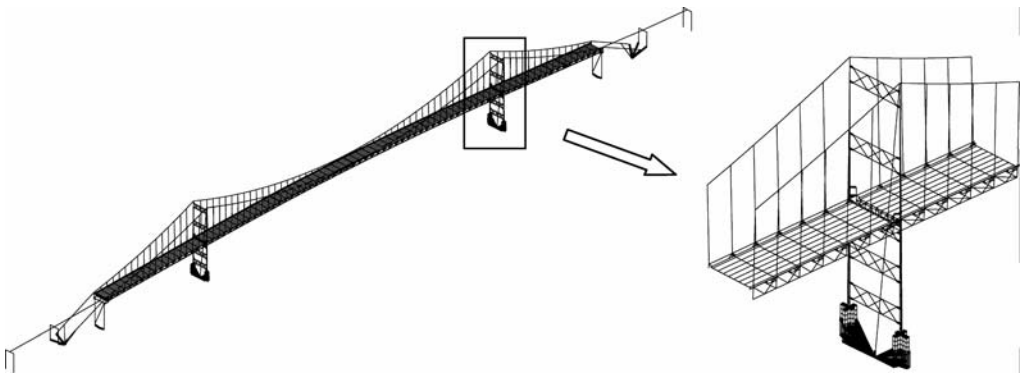

Fig. 3. Three-dimensional finite element model of Vincent Thomas Bridge.

Table 1
System identification results

	Natural frequency [Hz]		*Damping ratio (%)*			*Abdel-Ghaffar et al. (1992)*			
						Identified freq. [Hz]		*Computed freq. [Hz]*	
Mode no.	*Identified*	*Computed*	*Identified*	*Specified*	*MAC*	*Ambient*	*Earthquake*	*2D Model*	*3D Model*
1	0.214	0.231	3.8	1.8	0.961	0.216	0.209	0.197	0.201
2	0.226	0.226	2.3	1.8	0.711	0.234	0.224	0.221	0.224
3	0.357	0.364	0.9	1.6	0.928	0.366	0.364	0.348	0.336
4	0.455	0.459	2.6	1.7	0.988	0.487	0.448	0.459	0.443
5	0.514	0.511	2.1	1.8	0.995	0.494	0.513	0.455	0.438
6	0.576	0.571	0.5	1.8	0.994	0.579	0.562	0.549	0.527
7	0.687	0.684	1.5	2.0	0.994	N/A	N/A	N/A	N/A
8	0.815	0.823	0.2	2.3	0.997	N/A	N/A	N/A	N/A

previously identified from actual ambient vibration data and earthquake records (Abdel-Ghaffar et al., 1992), and (2) the corresponding natural frequencies computed from other validated FE models of VTB (Abdel-Ghaffar et al., 1992). This comparison shows that the FE model of VTB used in this study captures reasonably well the dominant low-frequency vibration modes of this bridge.

In simulating the wind-induced response of VTB, the aerodynamic forces are assumed to act along the bridge deck only. The aerodynamic parameters are assumed to be invariant along the bridge axis and the variation of the aerodynamic characteristics due to static rotation of the bridge deck (under gravity loads and aerostatic forces due to mean wind velocity) is neglected for simplicity. The aerodynamic parameters introduced in Section 2.3 are used in the simulation. The buffeting forces are simulated based on the simulated equivalent wind velocity fluctuation time histories according to Equation (17). The statistical correlation between longitudinal and vertical wind velocity fluctuations is ignored so that the spatially discretized wind velocity field is simulated as the combination of two independent stochastic vector processes. The simulation of the wind velocity fluctuations, $u^{eq}(t)$ and $w^{eq}(t)$, is performed using the spectral representation method in conjunction with the fast Fourier transform technique (Deodatis, 1996; Cao et al., 2000). The wind spectra for the longitudinal and vertical wind velocity fields are taken as Kaimal's spectrum (Kaimal et al., 1972) and Panofsky's spectrum (Lumley and Panofsky, 1964), respectively, defined as

$$S_{uu}(\omega, z) = \frac{200 z u_*^2}{4\pi U(z)\left[1 + \dfrac{50\omega z}{2\pi U(z)}\right]^{5/3}} \tag{18a}$$

$$S_{ww}(\omega, z) = \frac{3.36 z u_*^2}{4\pi U(z)\left[1 + 10\left(\dfrac{\omega z}{2\pi U(z)}\right)^{5/3}\right]} \tag{18b}$$

where $u_* = kU(z)/\ln(z/z_0)$ = shear velocity of the wind flow in m/s; z_0 = roughness length in m; $k \approx 0.4$; and $U(z)$ = mean wind velocity in m/s at height z above the ground level. In this study, $z_0 = 0.07$ m, and the height of the bridge deck above the ground is $z = 60$ m. The mean wind velocity, U, is taken as 10 m/s (36 km/h) to simulate wind-induced ambient vibrations under common low wind intensity. The coherence function of the wind velocity fluctuations at two different locations of abscissas x_1 and x_2 along the bridge deck is taken as (Davenport, 1968; Cao et al., 2000)

$$Coh_r(x_1, x_2, \omega) = \exp\left(-\frac{\lambda\omega|x_1 - x_2|}{2\pi U(z)}\right),\ \omega > 0 \tag{19}$$

where subscript $r = u$ or w, $\lambda = 10$ for the longitudinal wind velocity fluctuation and $\lambda = 8$ for the vertical wind velocity fluctuation. The aerodynamic forces are discretized at 27 locations along the bridge axis as shown in Figure 4, implying that the longitudinal and vertical stochastic wind velocity fields are discretized into two independent vector processes of 27 components each. Two-hour long wind velocity records are simulated with

Fig. 4. Locations of spatially discretized aerodynamic forces ("aerodynamic" nodes) along the bridge deck.

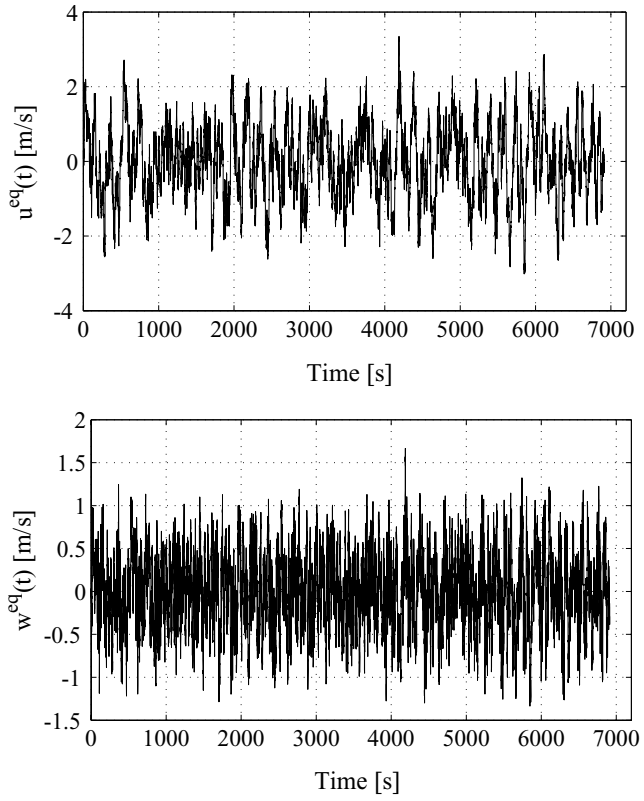

Fig. 5. Simulated longitudinal, $u^{eq}(t)$, and vertical, $w^{eq}(t)$, wind velocity fluctuations (U = 10 m/s).

a sampling time of $\Delta t = 0.25$ s. As illustration, Figure 5 shows a sample of the simulated longitudinal and vertical wind velocity fluctuation at the center point of the main span. The estimated (from simulated time histories) equivalent power spectral density function of the longitudinal wind velocity fluctuation is compared in Figure 6 to the theoretical wind spectrum (see Equations (16a) and (18a)) used to simulate the stochastic wind velocity field. Similarly, Figure 7 shows a comparison

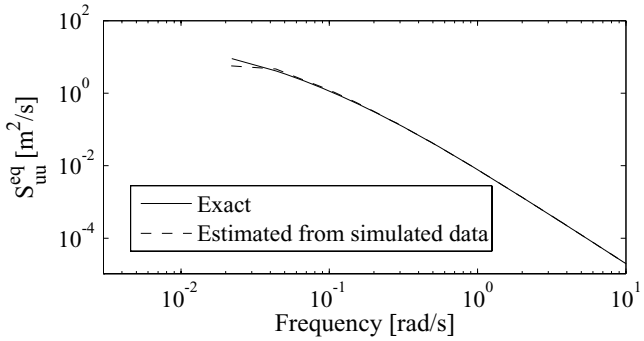

Fig. 6. Comparison of estimated (from simulated data) and exact longitudinal wind velocity spectrum.

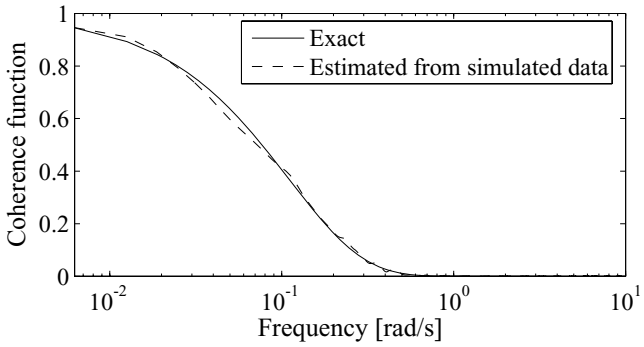

Fig. 7. Comparison of simulated and exact coherence function of the longitudinal wind velocity fluctuation.

between exact and estimated (from simulated time histories) coherence functions of the longitudinal wind velocity fluctuations at two stations located 28.4 m apart. From Figures 6 and 7, it is observed that the simulated wind velocity field along the bridge follows closely the assumed theoretical wind spectrum and coherence function.

It is assumed that the self-excited forces per unit span at different locations along an "aerodynamic" element of length L (corresponding to the tributary length of the "aerodynamic" node located at the center of the "aerodynamic" element) are fully correlated, while the random fluctuation of the buffeting forces per unit span along an "aerodynamic" element is accounted for. It is assumed that the buffeting force components induced by the longitudinal, u, and vertical, w, wind velocity fluctuations are uncorrelated, because the statistical correlation between u and w is neglected. Based on the above assumptions, for example, the self-excited and buffeting lift force components acting at an "aerodynamic" node with tributary length L can be expressed as (Chen et al., 2000a)

$$L^e_{se}(t) = L^c_{se}(t)L \tag{20a}$$

$$L^e_b(t) = L\int_0^t [h_{Lbu}(t-\tau)L^c_{bu}(\tau) + h_{Lbw}(t-\tau)L^c_{bw}(\tau)]\,d\tau \tag{20b}$$

where the superscript c indicates the center location of the "aerodynamic" element e; $h_{Lbu}(t)$ and $h_{Lbw}(t)$ are impulse response functions, the Fourier transforms of which, $H_{Lbu}(\omega)$ and $H_{Lbw}(\omega)$ satisfy the following relation:

$$|H_{Lbr}(\omega)|^2 = \frac{1}{L^2}\int_0^L\int_0^L coh_{Lbr}(x_1, x_2, \omega)\,dx_1\,dx_2 \tag{21}$$

in which $r = u$ *or* w; and $coh_{Lbr}(x_1, x_2, \omega)$ denotes the coherence function of the lift buffeting force components per unit span at two different positions x_1 and x_2 along

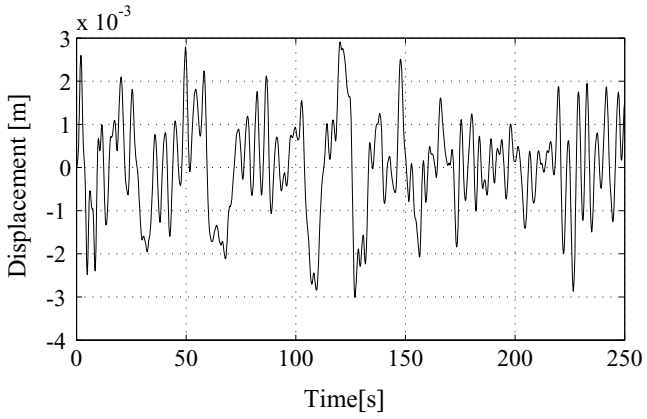

Fig. 8. Simulated vertical displacement response of VTB at center of main span.

the "aerodynamic" element, which is assumed to be the same as that for the wind velocity fluctuations (see Equation (19)). The drag and moment buffeting force components can be expressed in a similar way. The transfer functions $H_{L_{br}}(\omega)$ $(r = u, w)$ in Equation (21) are also approximated using rational functions for the purpose of time domain analysis, for example,

$$H_{L_{br}}(\omega) = \left[C_1 + \sum_{k=2}^{n} C_k \frac{i\omega}{d_k \dfrac{U}{B} + i\omega} \right] \tag{22}$$

where the coefficients C_k and d_k are determined through least squares fitting.

The dynamic response of a suspension bridge depends on the deformed bridge configuration and stress state under gravity loads. Therefore, first a geometric nonlinear static analysis is performed for the bridge under gravity loads only, using an incremental-iterative solution procedure. The aerodynamic wind forces (with buffeting forces based on the fluctuating wind velocity fields $u(t)$ and $w(t)$ and self-excited forces computed based on the displacement field of the bridge relative to its static equilibrium position under gravity loads only) are then applied with initial conditions given by the bridge state under gravity loads only. The dynamic equations of motion of the bridge under aerodynamic wind loads are linearized (geometrically) about the displacement and stress fields corresponding to gravity loads. Finally, these linearized equations of motion are solved using the constant average acceleration version of the Newmark time stepping method with parameters $\delta = 0.5$ and $\alpha = 0.25$. As an illustration, Figure 8 shows the simulated vertical dynamic response of the bridge at the center of the main span.

4 SYSTEM IDENTIFICATION OF VINCENT THOMAS BRIDGE

4.1 Data-driven stochastic subspace identification

Data-driven stochastic subspace identification (SSI-DATA) is one of the most advanced state-of-the-art output-only system identification methods, which has already been successfully applied for modal parameter identification of long-span bridges based on ambient vibration data. The SSI-DATA algorithm extracts a linear state-space model of the system considered using output-only measurement data directly (Van Overschee and De Moor, 1996; Peeters and De Roeck, 2001). Compared to two-stage time-domain system identification methods such as covariance-driven stochastic subspace identification (SSI-COV) (Van Overschee and De Moor, 1996) and the natural excitation technique (NExT) (James et al., 1993) combined with the eigensystem realization algorithm (ERA) (Juang and Pappa, 1985), SSI-DATA does not require any pre-processing of the data to calculate auto/cross-correlation functions or auto/cross-spectra of output data (i.e., SSI-DATA is a one-stage system identification method). In addition, robust numerical techniques such as QR factorization, singular value decomposition (SVD), and least squares are involved in this method. A brief review of this method is presented next.

The discrete-time state-space representation of a linear time-invariant system of order n is defined as

$$\mathbf{z}(k+1) = \mathbf{A}\mathbf{z}(k) + \mathbf{B}\mathbf{u}(k) \tag{23a}$$

$$\mathbf{x}(k) = \mathbf{C}\mathbf{z}(k) + \mathbf{D}\mathbf{u}(k) \tag{23b}$$

where $\mathbf{A} \in \mathbb{R}^{n\times n}$, $\mathbf{B} \in \mathbb{R}^{n\times l}$, $\mathbf{C} \in \mathbb{R}^{m\times n}$, $\mathbf{D} \in \mathbb{R}^{m\times l}$ = state space matrices in discrete form; $\mathbf{z}(k) \in \mathbb{R}^n$ = state vector; $\mathbf{u}(k) \in \mathbb{R}^l$ = load vector (vector of loading functions); and $\mathbf{x}(k) \in \mathbb{R}^m$, a column vector of size m (= number of measured/output channels) which represents the measured system response at discrete time $t = k(\Delta t)$ along m DOFs. In practical applications, the load vector input function $\mathbf{u}$ is often unknown/unmeasured and only the response of the structure is measured. In this case, the discrete-time state-space model in Equation (23) is extended to the following stochastic version:

$$\mathbf{z}(k+1) = \mathbf{A}\mathbf{z}(k) + \mathbf{w}(k) \tag{24a}$$

$$\mathbf{x}(k) = \mathbf{C}\mathbf{z}(k) + \mathbf{v}(k) \tag{24b}$$

where state matrices $\mathbf{A}$ and $\mathbf{C}$ are the same as in Equations (23): $\mathbf{A}$ = state transition matrix, which completely characterizes the dynamics of the system through its eigenproperties, and $\mathbf{C}$ = output matrix that specifies how the inner states are transformed into the measured

system response/output; $\mathbf{w}(k) \in \mathbb{R}^n$ = process noise due to external disturbances, modeling inaccuracies (i.e., missing high-frequency dynamics) and unknown input excitation (undistinguishable from the external disturbances); and $\mathbf{v}(k) \in \mathbb{R}^m$ = measurement noise due to sensor inaccuracies and also unknown input excitation (feed-through term). Both noise terms $\mathbf{w}(k)$ and $\mathbf{v}(k)$ are assumed to be zero-mean, white vector sequences with the following covariance matrix:

$$E\left[\begin{pmatrix}\mathbf{w}(i)\\ \mathbf{v}(i)\end{pmatrix}\begin{pmatrix}\mathbf{w}(j)^T & \mathbf{v}(j)^T\end{pmatrix}\right] = \begin{bmatrix}\mathbf{Q} & \mathbf{S}\\ \mathbf{S}^T & \mathbf{R}\end{bmatrix}\delta_{ij} \quad (25)$$

where $E[\dots]$ denotes the mathematical expectation operator; δ_{ij} = Kronecker delta; and $\mathbf{Q}, \mathbf{R}, \mathbf{S}$ = process and measurement noise auto/cross-covariance matrices.

The SSI-DATA procedure of extracting the state-space matrices $\mathbf{A}$ and $\mathbf{C}$ from output-only data can be summarized as follows: (1) Form an output Hankel matrix and partition it into "past" and "future" output submatrices. (2) Calculate the orthogonal projection matrix of the row space of the "future" output submatrix into the row space of the "past" output submatrix using QR factorization. (3) Obtain the system observability matrix and Kalman filter state estimate via SVD of the projection matrix. (4) Using the available Kalman filter state estimate, extract the discrete-time system state-space matrices as a least squares solution. To increase the computational efficiency of the system identification procedure, only the reference "past" outputs (outputs from the "reference" sensors) instead of all "past" outputs are used to form the output Hankel matrix (Peeters and De Roeck, 1999). Once the system state-space matrices are determined, the modal parameters (natural frequencies and damping ratios) of the $N = n/2$ vibration modes can be obtained as

$$\omega_i = |\ln(\lambda_{2i})/\Delta t| \text{ and } \xi_i = -\cos(\text{angle}(\ln(\lambda_{2i}))),$$
$$i = 1, 2, \dots, N \quad (26)$$

where $\lambda_i = i^{\text{th}}$ eigenvalue of matrix $\mathbf{A}$ and Δt = sampling time. It should be noted that λ_{2i-1} and λ_{2i} ($i = 1, 2, \dots, N$) are complex conjugate pairs, each pair corresponding to a vibration mode, that is, the natural frequency and damping ratio obtained from λ_{2i-1} are the same as those obtained from λ_{2i}. The vibration mode shapes are obtained as

$$\boldsymbol{\phi}_i = \mathbf{C} \cdot \mathbf{T}_{2i-1} \quad (27)$$

where $\mathbf{T}_i$ denotes the i^{th} eigenvector of matrix $\mathbf{A}$. Similarly, $\mathbf{T}_{2i-1}$ and $\mathbf{T}_{2i}$ ($i = 1, 2, \dots, N$) are complex conjugate pairs of eigenvectors, each pair corresponding to a vibration mode.

4.2 System identification results

A simulated array of 42 channels (21 along each side of the bridge deck) of vertical acceleration response of the bridge subjected to wind excitation is used for system identification. The simulated wind aerodynamic forces correspond to a mean wind velocity $U = 10$ m/s (36 km/h). Figure 9 shows the virtual accelerometer array along the bridge deck. The simulated acceleration records used in the identification process are 250-s long with a sampling rate of 20 Hz, corresponding to 5,000 samples per record/channel and a Nyquist frequency $f_{Nyq} = 10$ Hz. In applying SSI-DATA, these simulated acceleration data were first low-pass filtered using a finite impulse response (FIR) filter of order 512 with a cut-off frequency at 1.0 Hz. Then, an output Hankel matrix is formed including 100 block rows based on these low-pass filtered vibration data. The 15 channels on the east side of the main span are used as reference "past" output channels.

The identified natural frequencies and damping ratios are reported in Table 1 together with the corresponding computed natural frequencies and specified damping ratios of the VTB FE model used in this study. Table 1 also provides modal parameters obtained from previous system identification studies of VTB based on actual ambient vibration data and earthquake records (Abdel-Ghaffar et al., 1992). It is observed that there is an excellent agreement between the identified natural frequencies based on the simulated wind-induced response data and those computed from the bridge FE model. The difference between identified and analytically predicted natural frequency is largest for the first mode, which could be because the FE model of VTB used here has three very closely spaced modes with natural frequencies of 0.182, 0.226, and 0.231 Hz. The vibration mode at 0.182 Hz could not be accurately identified based on the simulated accelerometer data. The damping ratios identified based on the simulated wind-induced response data and the damping ratios specified in the FE model of VTB are in a good agreement considering that the estimation uncertainty of damping ratios is inherently larger than that of natural frequencies.

Fig. 9. Virtual array of accelerometers along the bridge deck.

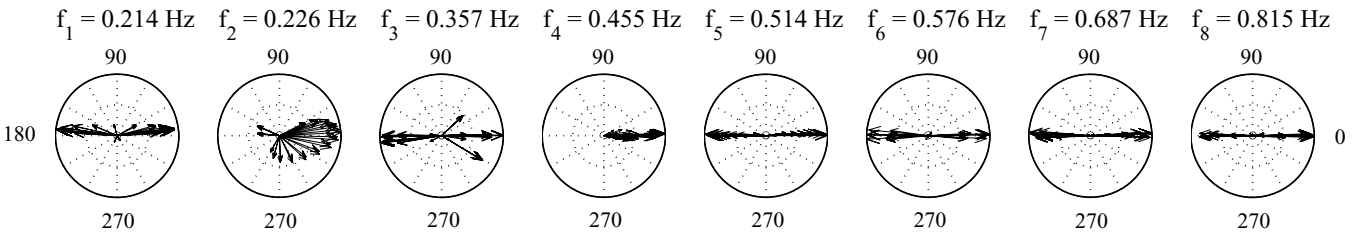

Fig. 10. Polar plot representation of vibration mode shapes identified using SSI-DATA.

It is important to mention that the identified natural frequencies and damping ratios also include the contribution of the aerodynamic stiffness and damping induced by the wind–structure interaction, which depend on the reduced wind velocity ($2\pi U/B\omega$), the geometrical configuration of the bridge section and the approach wind flow. Due to wind–structure interaction, the identified modal parameters (especially the damping ratios) of long-span cable-supported bridges under wind loading can vary significantly with wind velocity when approaching the flutter onset velocity. In a hybrid experimental-analytical flutter analysis of the Jianyin Bridge, a suspension bridge with a main span of 1,385 m and a streamlined closed box steel girder (36.8-m wide and 3-m high), modal aerodynamic damping ratios of some vibration modes reached values of approximately up to 10% (from corresponding structure modal damping ratios of 0.5%) at the flutter onset wind velocity (Ding et al., 2002). More studies about effects of wind–structure interaction on dynamic characteristics of long-span cable-supported bridges can be found in Matsumoto et al. (1996), Miyata et al. (1997), Larsen (1998), Chen et al. (2000a, 2000b, 2001), Matsumoto et al. (2002), and Chen and Kareem (2003).

The vibration mode shapes the identified using state-space model based system identification methods such as SSI-DATA are in general complex valued. Figure 10 represents in polar plots (i.e., rotating vectors in the complex plane) the mode shapes of VTB identified using SSI-DATA based on the simulated (wind-induced) ambient vibration data. These polar plots have the advantage to show directly the extent of the nonproportional damping characteristics of a vibration mode. If all complex valued components of a mode shape vector are collinear (i.e., in phase or 180 degrees out of phase), this vibration mode is said to be classically (or proportionally) damped. On the other hand, the more these mode shape components are scattered in the complex plane, the more the vibration mode is nonclassically (or nonproportionally) damped. However, measurement noise, estimation errors, modeling errors, and aerodynamic damping can also cause a truly classically damped mode to be identified as nonclassically damped. Figure 10 shows that most of the vibration modes (modes #1, 4–8) identified in this

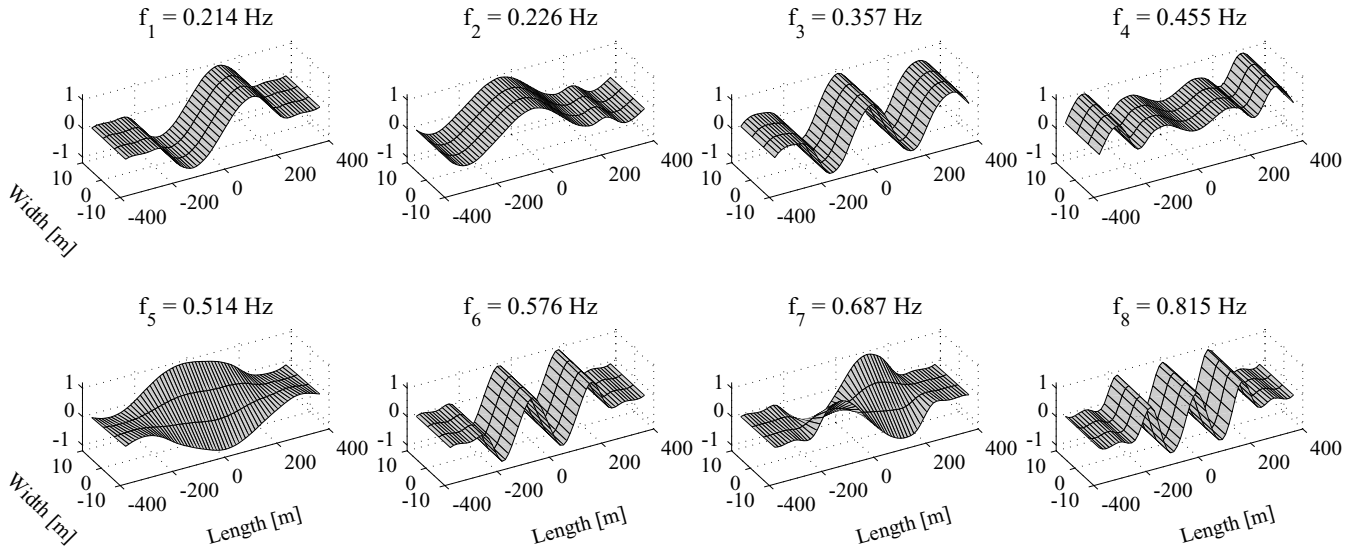

Fig. 11. 3D representation of normalized vibration mode shapes identified using SSI-DATA.

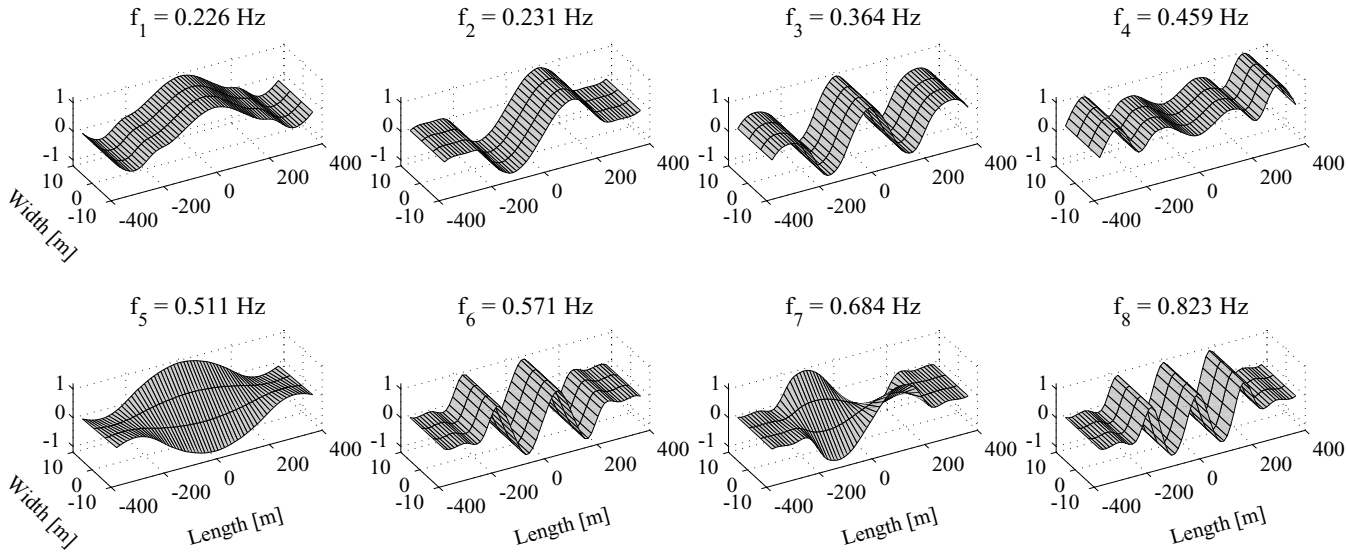

Fig. 12. 3D representation of vibration mode shapes computed from the finite element model of VTB.

study are either perfectly or nearly classically damped. A 3D representation of the normalized mode shapes of the bridge deck for these identified vibration modes is given in Figure 11. Normalization was performed by projecting all mode shape components onto their principal axis (in the complex plane) and then scaling this projected mode shape vector for a unit value of its largest component. The identified space-discrete mode shapes were interpolated between the virtual sensor locations using cubic splines along both sides of the bridge deck and straight lines across the deck.

The modal assurance criterion (MAC) (Allemang and Brown, 1982) is used to compare the identified and computed ("exact") vibration mode shapes. The MAC value, bounded between 0 and 1, measures the degree of correlation between corresponding identified and computed mode shapes as

$$\mathrm{MAC}(\phi_{\mathrm{identified}}, \phi_{\mathrm{computed}}) = \frac{|\phi^{*}_{\mathrm{identified}}\phi_{\mathrm{computed}}|^2}{|\phi_{\mathrm{identified}}|^2|\phi_{\mathrm{computed}}|^2} \tag{28}$$

where $*$ denotes the complex conjugate transpose. A MAC value of 0 indicates that the corresponding identified and computed mode shapes are completely uncorrelated, while a MAC value of 1 indicates perfect correlation between them. The MAC values for all pairs of identified and computed mode shapes are also given in Table 1. For all vibration modes identified, except for the second one, there is a very good-to-excellent agreement between corresponding identified and computed mode shapes. The high degree of nonclassical damping identified for the second mode (see Figure 10) could be the reason behind the low MAC value obtained for this mode. Such high degree of nonclassical damping could be true/physical (possibly due to wind–structure interaction) or could be caused by estimation and/or modeling errors. Three-dimensional representations of the mode shapes computed from the FE model of VTB are shown in Figure 12, which can be compared directly with their identified counterparts in Figure 11.

To study the effects of measurement noise on the system identification results, zero-mean Gaussian white noise processes are added to the simulated bridge vibration response data. Statistical properties (mean and standard deviation) of the estimated modal parameters are investigated for increasing levels of measurement noise. For this purpose, a set of 100 identifications was

Table 2
Mean and coefficient of variation (COV) of the identified natural frequencies normalized to their counterparts identified based on noise-free data at different measurement noise levels

	2% noise		*5% noise*		*10% noise*	
Mode no.	*Mean*	*COV (%)*	*Mean*	*COV (%)*	*Mean*	*COV (%)*
1	0.9998	0.05	0.9994	0.06	0.9992	0.07
2	1.0003	0.07	1.0000	0.09	0.9998	0.10
3	1.0005	0.03	1.0006	0.03	1.0008	0.04
4	0.9998	0.04	0.9997	0.05	0.9996	0.06
5	0.9999	0.01	0.9999	0.01	0.9999	0.02
6	0.9994	0.01	0.9992	0.01	0.9991	0.02
7	1.0001	0.01	1.0001	0.01	1.0001	0.01
8	1.0006	0.01	1.0007	0.01	1.0009	0.02

Table 3
Mean and coefficient of variation (COV) of the identified damping ratios normalized to their counterparts identified based on noise-free data at different measurement noise levels

	2% noise		*5% noise*		*10% noise*	
Mode no.	*Mean*	*COV (%)*	*Mean*	*COV (%)*	*Mean*	*COV (%)*
1	0.984	1.61	0.973	1.73	0.966	1.91
2	0.993	3.01	0.976	3.92	0.979	3.74
3	1.306	3.46	1.372	4.09	1.417	4.58
4	1.018	1.53	1.016	2.07	1.012	2.83
5	1.010	0.49	1.016	0.58	1.017	0.83
6	1.097	1.83	1.122	2.14	1.186	2.93
7	1.007	0.28	1.011	0.47	1.018	0.70
8	1.275	2.21	1.308	2.92	1.375	3.53

performed at each of three different measurement noise levels (2%, 5%, and 10%). For a given output channel, the noise level is defined as the ratio (in percent) of the root mean square (RMS) of the added noise process to the RMS of the simulated acceleration response. The added measurement noise processes are assumed statistically independent across the output channels and over the 100 realizations considered. The statistics (mean and coefficient of variation) over 100 trials of the identified natural frequencies and damping ratios normalized to their counterparts identified based on simulated noise-free data are reported in Tables 2 and 3, respectively, for the three measurement noise levels considered. The coefficient of variation of a random variable is defined as the ratio of its standard deviation to its (absolute) expected value (mean). In addition, mean and mean ± one standard deviation of the identified natural frequencies and damping ratios normalized to their counterparts identified based on simulated noise-free data are represented graphically in Figures 13 and 14, respectively. Based on the results reported in Tables 2 and 3 and plotted in Figures 13 and 14, it is observed that both the bias and coefficient of variation of the identified natural frequencies and damping ratios introduced by the measurement noise increase with increasing noise level as expected. However, bias and coefficient of variation due to measurement noise remain very small (negligible) for the identified natural frequencies (see Table 2 and Figure 13). Although they are significantly larger for the identified damping ratios (see Table 3 and Figure 14), they remain relatively small as it is well known that the

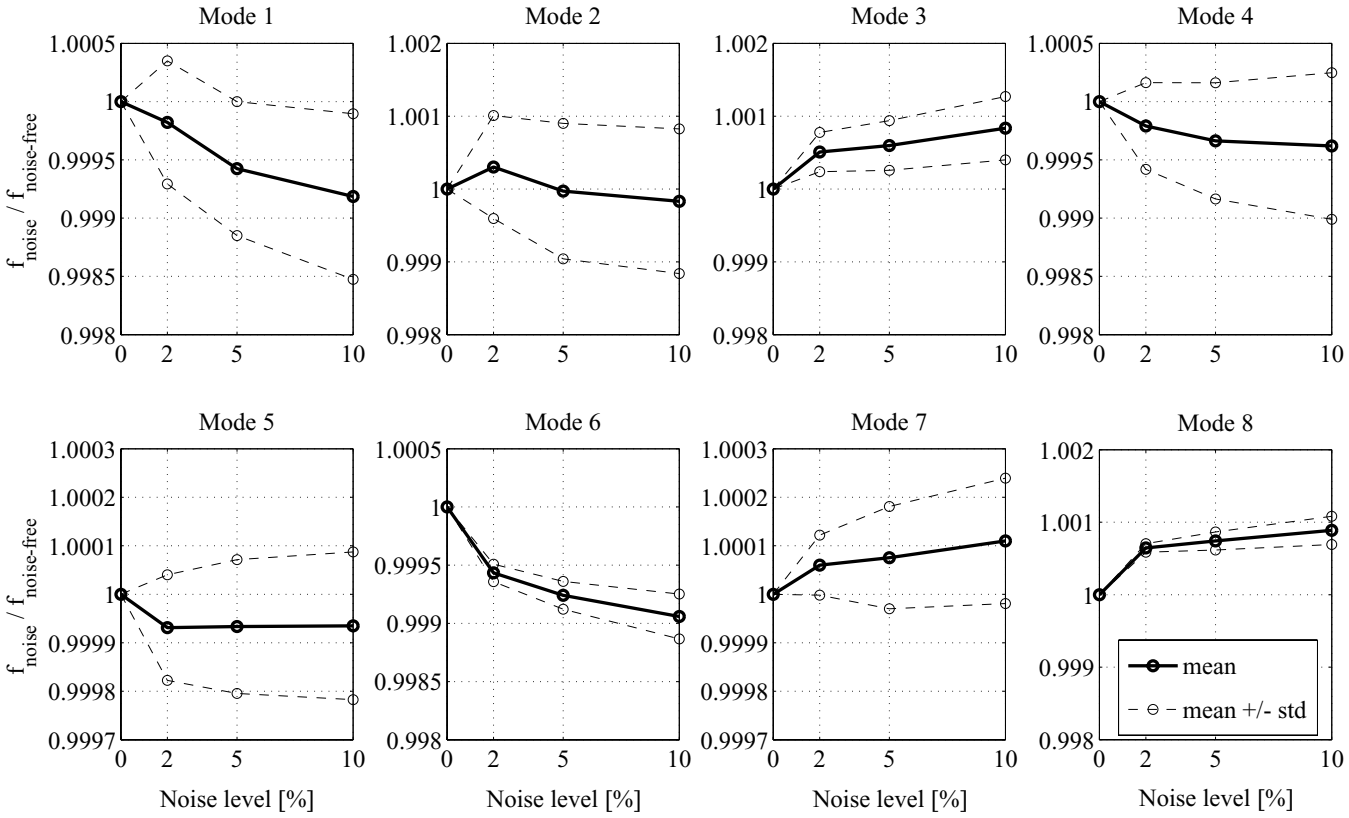

Fig. 13. Statistics (mean, mean ± one standard deviation) over 100 trials of the identified natural frequencies normalized to their counterparts identified based on noise-free data at different measurement noise levels.

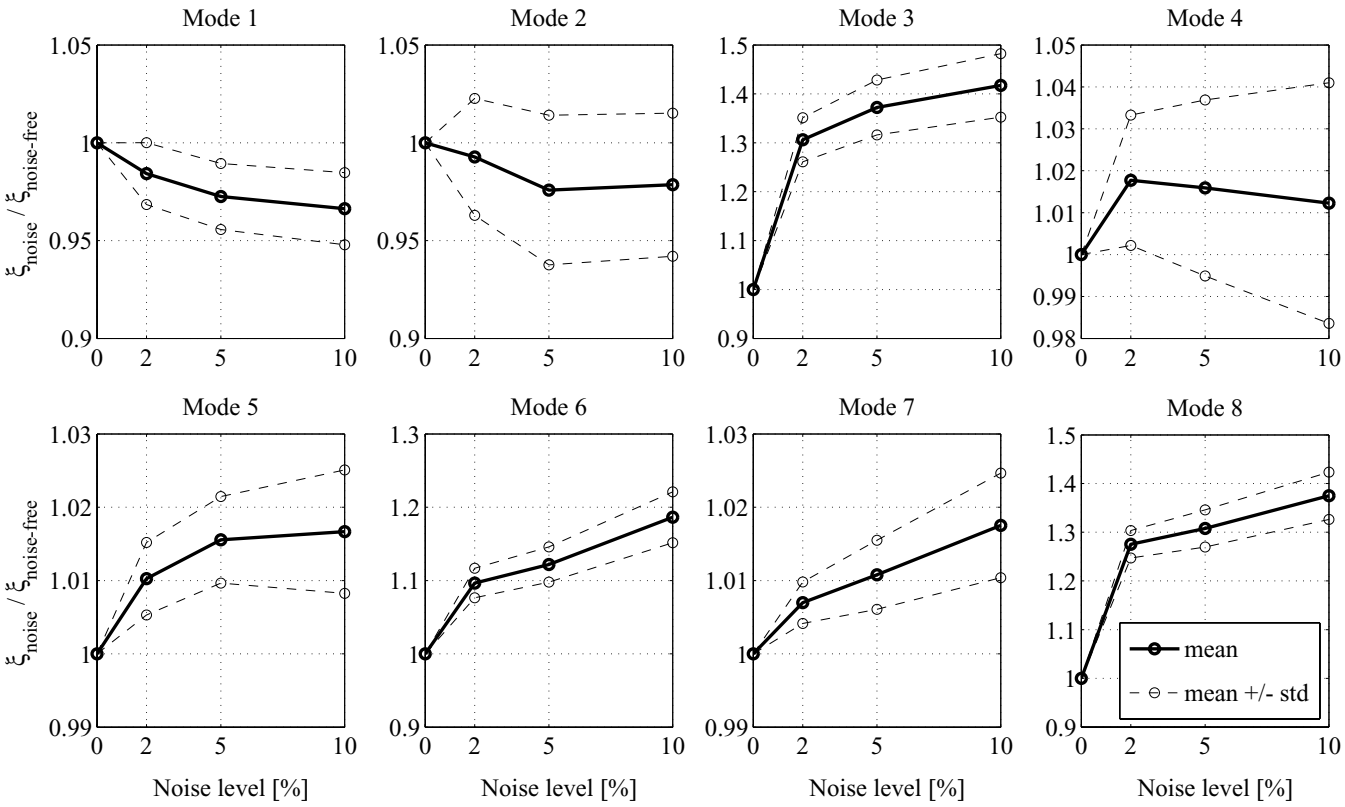

Fig. 14. Statistics (mean, mean ± one standard deviation) over 100 trials of the identified damping ratios normalized to their counterparts identified based on noise-free data at different noise levels.

estimation uncertainty of damping ratios is inherently larger than that of natural frequencies. It was also found that the measurement noise considered has very small (negligible) effects on the identified mode shapes.

5 CONCLUSIONS

Wind-induced ambient vibration of Vincent Thomas Bridge (VTB), a long-span suspension bridge located in San Pedro near Los Angeles, California, is simulated using a detailed three-dimensional FE model of the bridge and a state-of-the-art stochastic wind excitation model including both buffeting and self-excited forces. Based on these simulated ambient vibration data, modal parameters of the low-frequency vertical vibration modes of VTB are identified using data-driven stochastic subspace identification (SSI-DATA), a state-of-the-art output-only system identification method. The identified modal parameters are in good agreement with the computed ("exact") modal parameters obtained directly from the FE model of VTB, which themselves are in good agreement with the corresponding modal parameters of VTB identified by other researchers using actual ambient vibration data. This system identification study also provides the opportunity to investigate the accuracy of the modal identification results obtained using SSI-DATA in the case of a large and complex (virtual) structural problem for which the "exact" modal parameters (modal parameters of the FE model of VTB) are known, which is usually not the case when system identification methods are applied directly to real-world structures and data.

The effect of measurement noise on the identified modal parameters is investigated. Measurement noise is simulated by adding statistically independent zero-mean Gaussian white noise processes to the finite element simulated bridge response to wind excitation along a set of degrees of freedom (virtual output channels). The statistical properties (mean and coefficient of variation) of the identified modal parameters are investigated under an increasing measurement noise level. Both bias and coefficient of variation of the identified natural frequencies and damping ratios introduced by the measurement noise increase with increasing noise level as expected. However, bias and coefficient of variation due to measurement noise remain very small (negligible) for the identified natural frequencies. Although they are

significantly larger for the identified damping ratios, they remain relatively small as it is well known that the estimation uncertainty of damping ratios is inherently larger than that of natural frequencies.

The methodology and study presented in this article provide a validated framework for studying the effects of realistic damage scenarios in long-span cable-supported (suspension and cable-stayed) bridges (e.g., corrosion-induced losses in stiffness and strength of main cables and suspenders at different locations along the bridge) on modal identification results. These effects represent the basis for developing robust and reliable vibration-based structural health monitoring systems for long-span cable-supported bridges.

ACKNOWLEDGMENTS

This study was supported by the National Science Foundation under ITR Grant No. 0205720. The authors wish to express their thanks to Dr. Jon D. Raggett, President of West Wind Laboratory, Inc. and Dr. Xinzhong Chen at Texas Tech University for providing the aerodynamic parameters needed for the wind response simulation and for very useful suggestions and insightful discussions regarding the stochastic wind excitation model. Any opinions, findings, and conclusions or recommendations expressed in this article are those of the authors and do not necessarily reflect those of the sponsor.

REFERENCES

Abdel-Ghaffar, A. M., Masri, S. F. & Niazy, A. S. M. (1992), Seismic performance evaluation of suspension bridges, in *Proceedings of the 10th World Conference on Earthquake Engineering*, 4845–50.

ADINA R & D, Inc. (2002). Theory and modeling Guide Vol.1: ADINA, *Report ARD 02-7*, ADINA R&D, Inc., Watertown, MA.

Allemang, R. J. & Brown, D. L. (1982), A correlation coefficient for modal vector analysis, in *Proceedings of the 1st International Modal Analysis Conference*, Bethel, Connecticut, 110–116.

Cao, Y., Xiang, H. & Zhou, Y. (2000), Simulation of stochastic wind velocity field on long-span bridges, *Journal of Engineering Mechanics, ASCE*, **126**(1), 1–6.

Chen X. & Kareem, A. (2003), Aeroelastic analysis of bridges: Effects of turbulence and aerodynamic nonlinearities, *Journal of Engineering Mechanics, ASCE*, **129**(8), 885–95.

Chen, X., Kareem, A. & Matsumoto, M. (2001), Multimode coupled flutter and buffeting analysis of long span bridges, *Journal of Wind Engineering and Industrial Aerodynamics*, **89**(7), 649–64.

Chen, X., Matsumoto, M. & Kareem, A. (2000a), Time domain flutter and buffeting response analysis of bridges, *Journal of Engineering Mechanics, ASCE*, **126**(1), 7–16.

Chen, X., Matsumoto, M. & Kareem, A. (2000b), Aerodynamic coupling effects on flutter and buffeting of bridges, *Journal of Engineering Mechanics, ASCE*, **126**(1), 17–26.

Davenport, A. G. (1968), The dependence of wind load upon meteorological parameters, in *Proceedings of the International Research Seminar on Wind Effects on Buildings and Structures*, University of Toronto Press, Toronto, 19–82.

Deodatis, G. (1996), Simulation of ergodic multivariate stochastic processes, *Journal of Engineering Mechanics, ASCE*, **122**(8), 778–87.

Ding, Q., Chen, A. & Xiang, H. (2002), Coupled flutter analysis of long-span bridges by multimode and full-order approaches, *Journal of Wind Engineering and Industrial Aerodynamics*, **90**(12), 1981–93.

Doebling, S. W., Farrar, C. R., Prime, M. B. & Shevitz, D. W. (1996), Damage identification and health monitoring of structural mechanical systems from changes in their vibration characteristics: A literature review, *Los Alamos National Laboratory Report No. LA-13070-MS*, Los Alamos National Laboratory, Los Alamos, New Mexico.

Farrar, C. R. & Jauregui, D. A. (1998), Comparative study of damage identification algorithms applied to a bridge: I. Experiment, *Smart Materials and Structures*, **7**(5), 704–19.

Friswell, M. I. & Mottershead, J. E. (1995), *Finite element model updating in structural dynamics*, Kluwer Academic Publishers, Boston, MA.

James, G. H., Carne, T. G. & Lauffer, J. P. (1993), The natural excitation technique for modal parameters extraction from operating wind turbines, *Report No. SAND92-1666, UC-261*, Sandia National Laboratories, Sandia, New Mexico.

Juang, J. N. & Pappa, R. S. (1985), An eigensystem realization algorithm for modal parameter identification and model reduction, *Journal of Guidance, Control and Dynamics*, **8**(5), 620–27.

Kaimal, J. C., Wyngaard, J. C., Izumi, Y. & Cote, O. R. (1972), Spectral characteristics of surface-layer turbulence, *Journal of Royal Meteorological Society*, **98**(417), 563–89.

Larsen, A. (1998), Advances in aeroelastic analysis of suspension and cable-stayed bridges, *Journal of Wind Engineering and Industrial Aerodynamics*, **74**, 73–90.

Lazzari, M., Vitaliani, R. V. & Saetta, A. V. (2004), Aeroelastic forces and dynamic response of long-span bridges, *International Journal for Numerical Methods in Engineering*, **60**(6), 1011–48.

Liepmann, H. W. (1952), On the application of statistical concepts to the buffeting problem, *Journal of Aeronautical Science*, **19**(12), 793–800.

Lin, Y. K. & Yang, J. N. (1983), Multimode bridge response to wind excitations, *Journal of Engineering Mechanics, ASCE*, **109**(2), 586–603.

Lumley, J. L. & Panofsky, H. A. (1964), *The Structure of Atmospheric Turbulence*, Wiley-Interscience, New York.

Maeck, J. & De Roeck, G. (1999), Dynamic bending and torsion stiffness derivation from modal curvatures and torsion rates, *Journal of Sound and Vibration*, **225**(1), 153–70.

Matsumoto, M., Kobayashi, Y. & Shirato, H. (1996), The influence of aerodynamic derivatives on flutter, *Journal of Wind Engineering and Industrial Aerodynamics*, **60**(1), 227–39.

Matsumoto, M., Shirato, H., Yagi, T., Shijo, R., Eguchi, A. & Tamaki, H. (2002), Effects of aerodynamic interferences between heaving and torsional vibration of bridge decks: The case of Tacoma Narrows Bridge, *Journal of Wind Engineering and Industrial Aerodynamics*, **91**(12), 1547–57.

Miyata, T., Yamada, H. & Kazama, K. (1997), Discussion on aeroelastic detail and control in the flutter occurrences of long-span bridges, *Journal of Wind Engineering and Industrial Aerodynamics*, **69**, 839–49.

Pandey, A. K. & Biswas, M. (1994), Damage detection in structures using changes in flexibility, *Journal of Sound and Vibration*, **169**(1), 3–17.

Pandey, A. K., Biswas, M. & Samman, M. M. (1991), Damage detection from changes in curvature mode shapes, *Journal of Sound and Vibration*, **145**(2), 321–32.

Peeters, B. & De Roeck, G. (1999), Reference-based stochastic subspace identification for output-only modal analysis, *Journal of Mechanical Systems and Signal Processing*, **13**(6), 855–78.

Peeters, B. & De Roeck, G. (2001), Stochastic system identification for operational modal analysis: A review, *Journal of Dynamic Systems, Measurement, and Control*, **123**(4), 659–67.

Roger, K. L. (1977), Airplane math modeling methods for active control design, *Tech. Report CP-228,* AGARD.

Salawu, O. S. (1997), Detection of structural damage through changes in frequency: A review, *Engineering Structures*, **19**(9), 718–23.

Scanlan, R. H. (1978a), The action of flexible bridges under the wind. I: Flutter theory, *Journal of Sound and Vibration*, **60**(2), 187–99.

Scanlan, R. H. (1978b), The action of flexible bridges under the wind. II: Buffeting theory, *Journal of Sound and Vibration*, **60**(2), 201–11.

Shi, Z. Y., Law, S. S. & Zhang, L. M. (2002), Improved damage quantification from elemental modal strain energy change, *Journal of Engineering Mechanics, ASCE*, **128**(5), 521–29.

Simiu, E. & Scanlan, R. H. (1996), *Wind Effects on Structures: Fundamentals and Applications to Design*, John Wiley and Sons, New York.

Sohn, H., Farrar, C. R., Hemez, F. M., Shunk, D. D., Stinemates, D. W. & Nadler, B. R. (2003), A review of structural health monitoring literature: 1996–2001, *Los Alamos National Laboratory Report No. LA-13976-MS*, Los Alamos National Laboratory, Los Alamos, New Mexico.

Teughels, A. & De Roeck, G. (2004), Structural damage identification of the highway bridge Z24 by FE model updating, *Journal of Sound and Vibration*, **278**(3), 589–610.

Van Overschee, P. & De Moor, B. (1996), *Subspace Identification for Linear Systems*, Kluwer Academic Publishers, Norwell, Massachusetts.